analytical chemistry

Article

Cite This: *Anal. Chem.* 2020, 92, 1811−1817

pubs.acs.org/ac

Encapsulation and Release of Recognition Probes Based on a Rigid Three-Dimensional DNA "Nanosafe-box" for Construction of a Electrochemical Biosensor

Min Qing,[†,‡] Shengliang Chen,[†] Shunbi Xie,[‡] Ying Tang,[*,‡] Jin Zhang,[‡] and Ruo Yuan[*,†]

[†]Key Laboratory of Luminescent and Real-Time Analytical Chemistry (Southwest University), Ministry of Education, College of Chemistry and Chemical Engineering, Southwest University, Chongqing 400715, P. R. China

[‡]Chongqing Key Laboratory of Environmental Materials and Remediation Technologies (Chongqing University of Arts and Sciences), Chongqing University of Arts and Sciences, Chongqing 402160, P. R. China

Supporting Information

ABSTRACT: Herein a rigid three-dimensional (3D) DNA "nanosafe-box" (DNB) for encapsulation and release of a recognition probe (N_3) is designed to construct an electrochemical biosensor with the use of electroactive two-dimensional metal−organic framework (2D MOF) nanosheets as signal tags for ultrasensitive detection of mercury ion (Hg^{2+}). Initially, N_3 is locked in the 3D cavity of DNB by blocker DNA. After addition of target Hg^{2+}, exonuclease III (Exo-III) digestion is initiated to the liberate DNA "key" (K); thereby, the free K triggers a strand displacement reaction for exposing the prelocked N_3 to successfully ligate dibenzocyclooctyne (DBCO)-tagged anchor via metal-catalyst-free click chemistry, in which amounts of 2D MOF nanosheets containing Co(II) as electron mediator are introduced accompanied by significant electrochemical response. Compared with traditional linear or stem-loop DNA nanostructure, the well-designed 3D DNB possesses remarkably enhanced mechanical rigidity and structural stability, resulting in improved accessibility of probes and increased loading amounts of signal tags. More importantly, by this way of encapsulation and release of recognition probes, the background signal is decreased dramatically, leading to increased sensitivity of the proposed biosensor. Consequently, this electrochemical biosensor exhibits outstanding analytical performance for Hg^{2+} detection with a low detection limit of 33 fM and dynamic linear range of 0.1 pM to 10 nM. This strategy offers an ingenious method for detection of metal ions and biomarkers, possessing potential applications in environmental tests and clinical diagnosis.

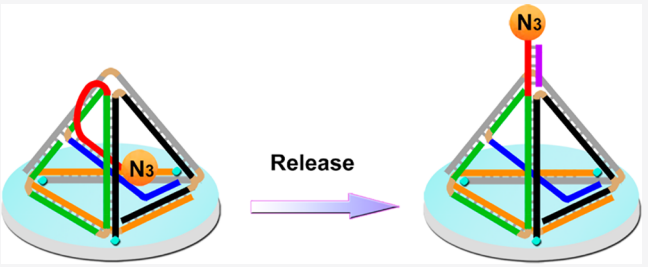

Owing to its easy programmability, highly predictable base-pairings, convenient synthesis, and biocompatibility, DNA has been harnessed to design and engineer DNA nanostructures with specific structures, outstanding functions, and programmable molecular recognition capacity.[1−5] Therefore, a wide variety of multifunctional DNA nanostructures, such as linear or stem-loop building blocks[6−13] or relatively rigid triplex−helix DNA nanostructures,[14−16] have been reported for biosensing based on conformational switching. Although the recognition element is partially hid for the steric hindrance effect, these nonrigid DNA nanostructures with variable surface orientation may cause entanglement and locally aggregate between the probes, resulting in decreased analytical performance. Moreover, it is found that the conformation of stem-loop DNA is greatly perturbed at solid surfaces relative to homogeneous solutions, leading to reduced recognition properties and rates of folding and unfolding to some extent.[17,18] In light of the above shortcomings, the tetrahedral DNA nanostructure is a typical three-dimensional (3D) DNA scaffold that can improve the accessibility of probes and increase the loading amounts of signal tags, owing to its characteristics of remarkably enhanced mechanical rigidity and structural stability and well-controlled orientation.[19−23] Nevertheless, because the recognition probe is exposed to the surface of the tetrahedral DNA nanostructure, it is inevitable to increase nonspecific interactions and background signal, resulting in decreased sensitivity. Therefore, in this work, we set out to design a 3D DNA "nanosafe-box" (DNB) to encapsulate the recognition probe in its 3D cavity and release it on demand, which not only enhances mechanical rigidity and structural stability compared with 1D or 2D DNA nanostructures but also dramatically lowers the background signal over previously reported 3D DNA nanostructures.

Mercury ion (Hg^{2+}), one of the most hazardous pollutants, can accumulate in the human body through drinking water, thereby causing neural damage.[24,25] Currently, various techniques have been reported for Hg^{2+} detection, such as atomic fluorescence spectrometry (AFS),[26] coupled plasma mass spectrometry (ICPMS),[27] fluorescence,[28,29] colorimetric

Received: August 8, 2019
Accepted: December 5, 2019
Published: December 5, 2019

DOI: 10.1021/acs.analchem.9b03627
Anal. Chem. 2020, 92, 1811−1817

Scheme 1. (A) Formation of Functionalized Porphyrin Paddlewheel Framework-3 Complex (anchor−Au NPs@PPF-3) and (B) Construction of the Electrochemical Biosensor Based on 3D DNA "Nanosafe-box"-Guided Encapsulation and Release of the Recognition Probe and the Detection Principle of Hg^{2+}

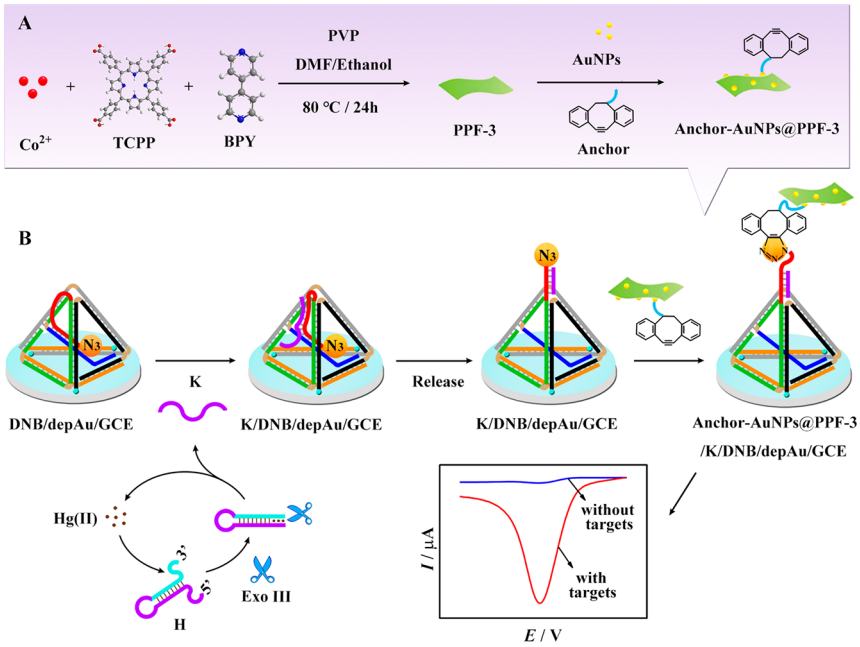

methods,[30,31] and electrochemical techniques.[32,33] These innovative methods generally possess high selectivity and sensitivity. Among these methods, the electrochemical technique, with advantages of excellent sensitivity, simple instrumentation, relatively low cost, and rapid response time, has experienced soaring popularity in Hg^{2+} assays.[34,35] Here an electrochemical biosensor based on a 3D DNB and electroactive 2D MOFs nanosheets was developed for ultrasensitive detection of Hg^{2+}. As illustrated in Scheme 1, the electrochemical biosensor was fabricated by directly immobilizing DNB on a gold nanoparticle-coated glassy carbon electrode (depAu/GCE) via gold−thiol contacts. Because the recognition probe (N_3) was locked by blocker DNA (B) appended to the 3D cavity of DNB, dibenzocyclooctyne (DBCO) was inhibited to interact with it. After addition of target Hg^{2+}, exonuclease III (Exo-III)-assisted target recycling reaction was initiated via forming sticky termini in the stem of the hairpin probe (H) with stable T−Hg^{2+}−T bonding, resulting in the release of the DNA "key" (K) and Hg^{2+}. In this regard, the released K was introduced into the surface of the electrode and triggered a strand displacement reaction to expose the N_3 prelocked in the 3D cavity of DNB. Thereafter, the free N_3 could bind with DBCO by metal-catalyst-free click chemistry and brought amounts of 2D MOF nanosheets containing Co(II) as electron mediator to the surface of electrode, leading to a significant electrochemical signal. By virtue of such design, the 3D DNB not only markedly enhances mechanical rigidity and structural stability for improving the accessibility of probes and increasing the loading amounts of signal tags but also is capable of encapsulating and releasing the recognition probe for minimizing the background signal, which can significantly improve the sensitivity for Hg^{2+} detection. Above all, this work affords an innovative and promising direction for the detection of metal ions and biomarkers, having potential application in the area of environmental tests and clinical diagnosis.

EXPERIMENTAL SECTION

Preparation of Anchor−Au NPs@PPF-3. First, the porphyrin paddlewheel framework-3 (PPF-3) is synthesized based on a hydrothermal method.[36] Then, photoreduction method is conducted to prepare gold nanoparticle-functionalized PPF-3 (AuNPs@PPF-3).[37] Subsequently, 50 μL of anchor (100 μM) was treated with 5 μL of 1 mM TCEP for reducing the disulfide bond. The activated anchor with thiol labeled at its 5′-terminus and dibenzocyclooctyne (DBCO) labeled at its 3′-terminus was then added into 500 μL of AuNPs@PPF-3 suspension and incubated at 4 °C overnight. Therefore, the anchor was immobilized on the surface of AuNPs@PPF-3 via the gold−thiol reaction, and the DBCO was exposed around the anchor−AuNPs@PPF-3 complex. Finally, the anchor−AuNPs@PPF-3 complex was obtained via centrifugation and stored at 4 °C before use.

Formation of DNA "Nanosafe-box" (DNB). Equal molar quantities of five oligonucleotides (T1, T2, T3, T4, and blocker), for the preparation of the DNB, were mixed in the assembly buffer at a final concentration of 2 μM and then heated to 95 °C for 10 min followed by slowly cooling to 4 °C in a thermal cycler. Thereafter, the mixture was diluted to 1 μM via hybridization buffer for the following experiment. For the polyacryamide gel electrophoresis (PAGE) assays, oligonucleotides without the thiol group are used and the preparation process is the same as mentioned above.

Preparation of Modified Electrode. Initially, the mirror-like glassy carbon electrode (GCE) was polished by alumina slurry, followed by rinsing thoroughly with ultrapure water. Subsequently, the AuNP layer (depAu) was coated onto the surface of the cleaned GCE by electrodeposition. Thereafter, 10 μL of above prepared DNB (1 μM) was dropped onto the above prepared depAu/GCE and then incubated at room temperature for 3 h. Following a gentle rinsing with washing buffer, the DNB-modified electrode (DNB/depAu/GCE) was stored at 4 °C before use.

DOI: 10.1021/acs.analchem.9b03627
Anal. Chem. 2020, 92, 1811−1817

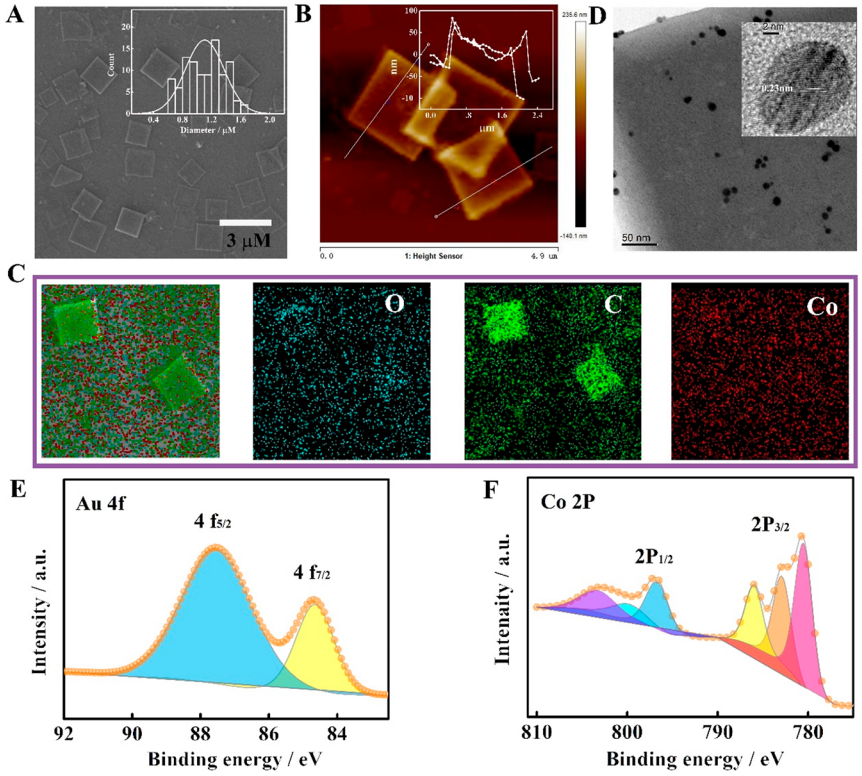

Figure 1. (A) FESEM images and size distribution (inset) of 2D PPF-3. (B) AFM images and thickness distribution (inset) of 2D PPF-3. (C) The corresponding elemental mappings of the region C, Co, and O elements. (D) Low- and (inset) high-magnification TEM images of AuNPs@PPF-3. (E) XPS spectra of Au 4f and (F) XPS spectra of Co 2p, which contain two spin−orbit doublets. The first one is at 780.5 and 796.7 eV and the second one at 782.9 and 800.0 eV. Two oxidation peaks at 786.0 and 803.2 eV are related to Co^{3+} and Co^{2+}, respectively.

Target Detection. The generation procedure of the DNA "key" (K) was conducted in a thermal cycler, and the details are as follows. First, 20 μL of hairpin probe (H, 2 μM) and 20 μL of various concentrations of Hg^{2+} were mixed in 1× Exo III reaction buffer at 25 °C for 20 min to form a sticky termini in the stem of the hairpin probe (H) by specific T−Hg^{2+}−T bonding. Then, 10 μL of Exo III (16 U/μL) was added and incubated at 37 °C for 20 min to release the single-stranded K. Finally, Exo III was inactivated by heating at 70 °C for 10 min. Afterward, 10 μL of single-stranded K was dropped onto the surface of above prepared DNB/depAu/GCE and incubated at 37 °C for 2 h to release the recognition probe (N_3) from the 3D cavity of DNB. Finally, 10 μL of anchor−AuNPs@PPF-3 complex was dropped onto the surface of DNB/depAu/GCE and incubated for 60 min. Therefore, the anchor−AuNPs@PPF-3 complex was immobilized onto the modified electrode surface via metal-catalyst-free click chemistry reaction of DBCO and N_3. Finally, the prepared biosensor was subjected to electrochemical measurements.

RESULTS AND DISCUSSION

Characteristics of the AuNPs@PPF-3 Complex. According to the field emission scanning electron microscopy (FE-SEM) and atomic force microscopy (AFM) characterization of 2D PPF-3, a square-like sheet structure with average lateral size of 1.1 μM (Figure 1A) and approximate thickness of 40 nm (Figure 1B) was observed. Energy-dispersive X-ray spectroscopy (EDS, Figure S1) and the corresponding elemental mapping (Figure 1C) of 2D PPF-3 from SEM revealed uniform dispersion of the C, Co, and O elements in the whole nanocomposite, and the atomic ratio of C:O:Co is 5.6:1.0:1.1. Powder X-ray diffraction (XRD) characterization was performed to confirm the crystal structure of 2D PPF-3. As shown in Figure S2A, the 2D PPF-3 showed an XRD pattern almost identical to that of the 3D bulk MOFs, indicating that they have the same crystal structure. Moreover, N_2 adsorption experiments indicated that 2D MOFs displayed a higher Brunauer−Emmett−Teller (BET) surface area (ca. 11.1648 m^3 g^{-1}), while that of the 3D bulk MOFs significantly decreased to 3.3560 m^3 g^{-1} (Figure S3), suggesting that 2D PPF-3 possesses more highly accessible active sites compared to 3D bulk MOFs. In this work, 2D PPF-3 with a superior redox property also served as a template for adherent Au NPs. The low- and high-resolution transmission electron microscopy (HRTEM) images verified the distribution of Au NPs on the 2D matrix (Figure 1D). In addition, the elemental analysis and chemical state of AuNPs@PPF-3 was collected by X-ray photoelectron spectroscopy (XPS). The Au $4f_{7/2}$ and Au $4f_{5/2}$ peaks appear at 84.6 and 87.5 eV (Figure 1E), respectively, indicating that Au NPs are only composed of metallic Au^0.[38] Figure 1F shows that the two characteristic peaks of the Co 2p spectrum corresponded to $2p_{3/2}$ and $2p_{1/2}$, respectively.[39] These results confirmed the successful synthesis of AuNPs@PPF-3 compounds.

Polyacrylamide Gel Electrophoresis (PAGE) Characterization. First, the stepwise formation of DNB is confirmed by 8% PAGE. As depicted in Figure 2A, lane 10 is a DNA marker (100bp to 600bp), and lanes 1 to 5 represent the single-strand of T1 (1 μM), T2 (1 μM), T3 (1 μM), T4 (1 μM), and blocker (1 μM), respectively. By successive addition of reactant DNA, a series of bright bands with stepwise increased molecular weight appeared (lane 6 to lane 9),

DOI: 10.1021/acs.analchem.9b03627
Anal. Chem. 2020, 92, 1811−1817

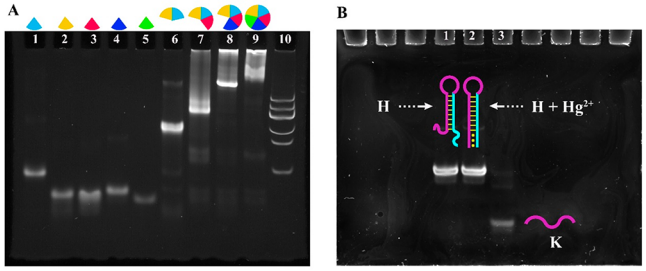

Figure 2. PAGE analysis for different samples: (A) lane 1, single-stranded DNA T1; lane 2, single-stranded DNA T2; lane 3, single-stranded DNA T3; lane 4, single-stranded DNA T4; lane 5, single-stranded DNA blocker; lane 6, annealing of T1 and T2; lane 7, annealing of T1, T2, and T3; lane 8, annealing of T1, T2, T3, and T4; lane 9, annealing of T1, T2, T3, T4, and blocker; lane 10, DNA marker (100bp to 600bp). (B) Lane 1, annealing of single-stranded H; lane 2, the mixture of single-stranded H and Hg^{2+}; lane 3, the mixture of single-stranded H, Hg^{2+}, and Exo III.

suggesting that DNB was formed. Moreover, the feasibility of signal amplification by Exo III-assisted target recycling was valuated (Figure 2B). Compared with single-strand H (lane 1), the reaction of H, target, and Exo III generated a band (single-stranded K) with lower molecular weight (lane 3), because the mononucleotides in the stem of H were stepwise removed by Exo III from the 3′-terminus. As a control test, only mixed H with Hg^{2+} (lane 2), the mobility of the band was consistent with H.

Electrochemical Characterization of the Modified Electrode. For characterizing the stepwise preparation process of the biosensor, cyclic voltammogram (CV) was recorded in $[Fe(CN)_6]^{3-/4-}$ solution. The current signal of $[Fe(CN)_6]^{3-/4-}$ at the depAu/GCE was significantly increased (Figure 3, curve b), compared with that at the bare GCE

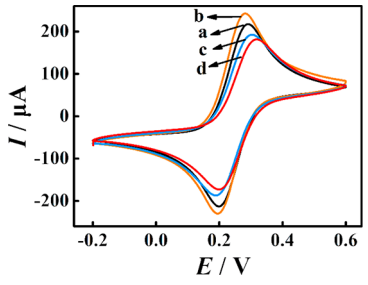

Figure 3. Cyclic voltammogram of (a) bare GCE, (b) depAu/GCE, (c) DNB/depAu/GCE, and (d) K/DNB/depAu/GCE.

(curve a). Conversely, when DNB was immobilized on the depAu/GCE, the current signal was obviously inhibited, owing to the repulsion effect between the negatively charged phosphate backbone of the DNA and $[Fe(CN)_6]^{3-/4-}$. After the single-stranded K was introduced onto the electrode, the current signal of $[Fe(CN)_6]^{3-/4-}$ decreased again. These results were also confirmed with electrochemical impedance spectroscopy (EIS, Figure S4) and revealed the successfully assembled biosensor.

Optimization of the Experimental Conditions. Exo III-assisted target recycling is highly dependent on Exo III; thus, the influence factors of Exo III activity are optimized by 8% PAGE. First, the molar ratio of enzyme to H in the reaction mixture was optimized (Figure 4A). The band in lane 1 represented the H (1 μM) with Hg^{2+} (10 nM). After addition of Exo III at concentrations of 5 or 10 units (U), the bands in lanes 2 and 3 appeared at the same position as the band in lane 1, demonstrating that the biodegradation rate of DNA by Exo III was slow in the constant reaction time. Once the concentration of Exo III was higher than 10 U, two new bands with low molecular weight were observed, corresponding to intermediate products and final resultants (K), respectively. With the increase of Exo III at concentrations from 15 to 40 U, the brightness of bands related to final resultants were gradually increased whereas that of the bands related to intermediate products decreased (lane 4−9). Therefore, 40 U of Exo III was chosen as optimal concentration. Thereafter, the effect of reaction temperature on the activity of Exo III was also investigated by 8% PAGE. As shown in Figure 4B, compared with the band of lane 1 (1 μM H and 10 nM Hg^{2+}), two new bands with lower molecular weight appeared in lanes 2 to 8, corresponding to intermediate products and final resultants (K), respectively. This illustrated that the mononucleotides in the stem of H were stepwise removed by Exo III in the presence of target Hg^{2+}. The brightness of the band related to final resultants increased with rising reaction temperature in the range of 15−37 °C and then decreased in the range of 40−45 °C. Thus, 37 °C was employed as the optimum temperature. Additionally, the gray scale intensity of bands is calculated by ImageJ, which were consistent with the results of gel electrophoresis (Figure 4C and 4D).

Analytical Performance of the Biosensor. By utilizing the 3D DNB for encapsulation and release of the recognition probe, the designed biosensor was used to quantitatively determine Hg^{2+} standards at various concentrations. Figure 5 displays that the differential pulse voltammetry (DPV) current response gradually increased with the increased Hg^{2+} concentration and depicts a good linearity with the logarithm (lg) of Hg^{2+} concentration from 0.1 pM to 10 nM. The linear regression equation can be expressed as I (μA) = −3.7658 − 2.2835 lg $C_{Hg^{2+}}$ (pM) with a correlation coefficient of 0.9955. Compared with other Hg^{2+} detection protocols (Table S2), this designed biosensor displayed superior sensitivity with a limit of detection (LOD) of 33 fM, attributed to the minimized background signal by the 3D DNA "nanosafe-box" as well as the enhanced electrochemical signal by electroactive 2D PPF-3 nanosheets.

Reproducibility, Stability, and Specificity of the Biosensor. For assessing the reproducibility, intraassays, and interassays are carried out. The relative standard deviations (RSDs) was 4.79% (n = 5) for intraassays and 4.58% (n = 5) for interassays, respectively, indicating a good reproducibility. In addition, a long-term assay is deployed to evaluate the stability of designed biosensor. The DPV current response decreased 19.45% after 20 days, proving that the biosensor had an acceptable stability (Figure 6A). As shown in Figure 6B, a series of interfering ions (Pb^{2+}, Mn^{2+}, Zn^{2+}, Ni^{2+}, Cu^{2+}, Co^{2+}, Fe^{3+}, and Cd^{2+}) with higher concentration were employed to assess the specificity of the platform to Hg^{2+}. A negligible DPV current response of interfering ions was observed, compared with that of target Hg^{2+} and mixture. These results indicated a good selectivity with anti-interference for this biosensor.

Practical Application. To assess the potential application of the proposed biosensor, the water samples (obtained from Chongde Lake at Southwest University in Chongqing) were monitored by the proposed biosensor and atomic fluorescence spectrometry (AFS). The Hg^{2+} level was calculated according

DOI: 10.1021/acs.analchem.9b03627
Anal. Chem. 2020, 92, 1811−1817

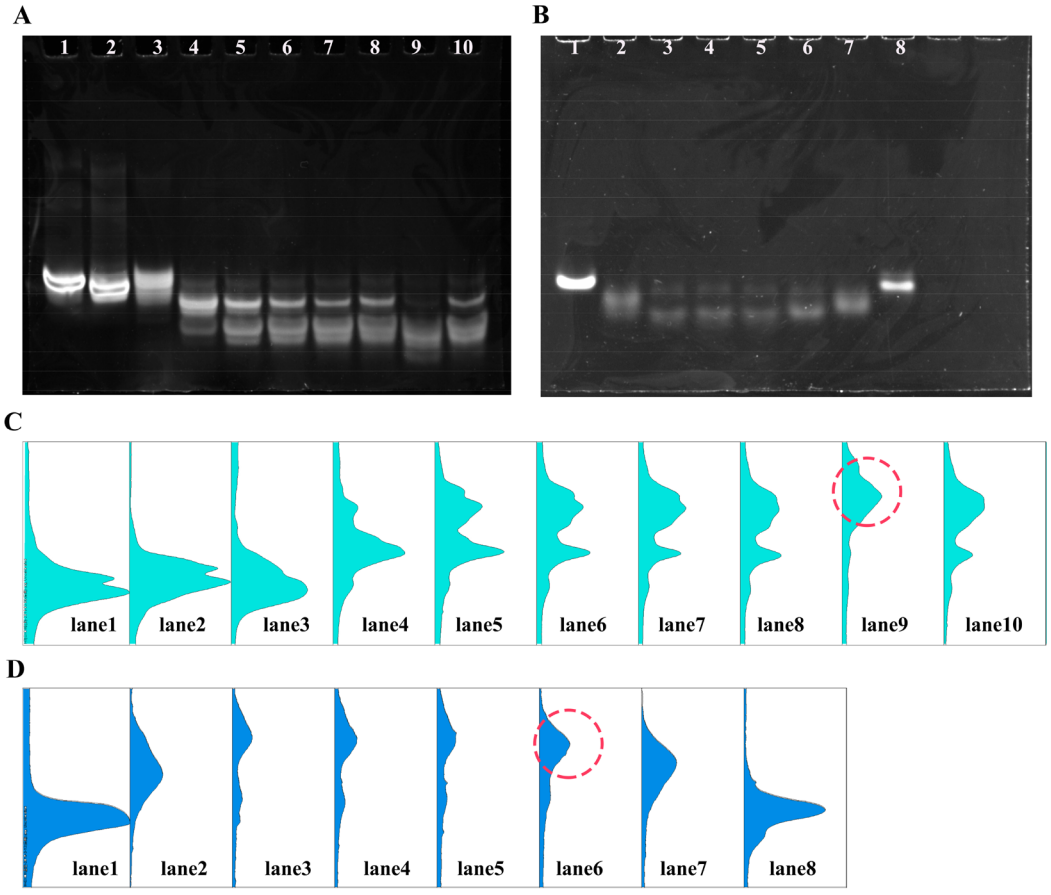

Figure 4. (A) Influence of the molar ratios between H and Exo III on activity of Exo III: lane 1, 1 μM, H; lane 2, 1 μM, H and 5 U Exo III; lane 3, 1 μM H and 10 U Exo III; lane 4, 1 μM H and 15 U Exo III; lane 5, 1 μM H and 20 U Exo III; lane 6, 1 μM H and 25 U Exo III; lane 7, 1 μM H and 30 U Exo III; lane 8, 1 μM H and 35 U Exo III; lane 9, 1 μM H and 40 U Exo III; lane 10, 1 μM H and 45 U Exo III. (B) Effect of reaction temperature on activity of Exo III: lane 1, 1 μM, H; lane 2 to lane 8 including 1 μM, H and 40 U Exo III in reaction temperature of 15 °C, 20 °C, 25 °C, 30 °C, 37 °C, 40 °C, 45 °C, respectively. (C) The gray scale intensity of part A. (D) The gray scale intensity of part B.

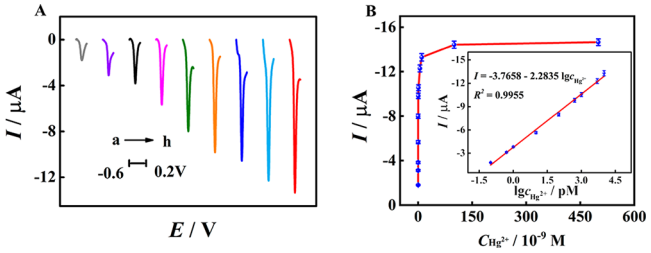

Figure 5. (A) DPV response of the biosensor with various concentrations of Hg^{2+} (0.1 pM, 0.5 pM, 1 pM, 100 pM, 500 pM, 1 nM, 5 nM, 10 nM). (B) Variance of the DPV response with the concentration of Hg^{2+} in the range of 0.1 pM to 500 nM. The inset shows the calibration plot of DPV response vs the logarithm of Hg^{2+} concentration in the range of 0.1 pM to 10 nM.

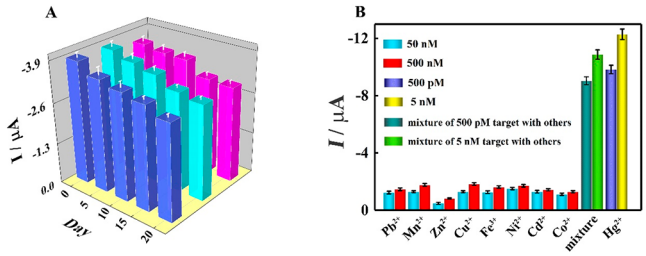

Figure 6. (A) Stability of the proposed biosensor (1 pM Hg^{2+}). (B) Specificity of the biosensor toward mixture control and different interferences: Pb^{2+}, Mn^{2+}, Zn^{2+}, Ni^{2+}, Cu^{2+}, Co^{2+}, Fe^{3+}, and Cd^{2+}. The concentration of each interfering ion was 100-fold more than that of target Hg^{2+} (500 pM and 5 nM).

to the equation I (μA) = −3.7658 − 2.2835 lg $c_{Hg}{}^{2+}$ (pM). As shown in Table 1, the proposed biosensor had potential for detecting Hg^{2+} in real samples.

CONCLUSIONS

In summary, this work designed a multifunctional 3D DNA "nanosafe-box" for encapsulating and releasing of recognition probe, which was applied in an electrochemical biosensor with use of electroactive 2D MOF nanosheets as signal tags for Hg^{2+} detection. The merits of this electrochemical biosensors were

Table 1. Recovery Results of the Proposed Biosensor in Tap Water

sample	dilution ratio	AFS found (nM)[a]	biosensor found (nM)[a]
1	10	0.10	0.11
2	5	0.45	0.48
3	2	1.10	1.29
4	0	2.15	1.93

[a]Mean value of three parallel determinations in the optimal experiment conditions.

DOI: 10.1021/acs.analchem.9b03627
Anal. Chem. 2020, 92, 1811−1817

reflected in the following aspects. First, the well-designed DNA "nanosafe-box" scaffold possessed markedly enhanced mechanical rigidity and structural stability, which could improve the accessibility of probes and increase the loading amounts of signal tags. Second, the encapsulation and release of recognition probes by the unique 3D DNA "nanosafe-box" could obviously lower the background signal, leading to significantly improved sensitivity. Third, in light of the higher surface area and more accessible active sites over previously reported 3D bulk MOFs, 2D MOFs were more conducive to transport electrons, which could improve the sensitivity of biosensor. Above all, this strategy opened a new horizon for detection of metal ions and biomarkers, having potential applications in environmental tests and clinical diagnosis.

■ ASSOCIATED CONTENT

Supporting Information

The Supporting Information is available free of charge at https://pubs.acs.org/doi/10.1021/acs.analchem.9b03627.

Chemicals and materials, apparatus, synthesis of bulk 3D metal−organic frameworks (MOFs), experimental measurements, preparation of polyacrylamide gel electrophoresis (PAGE), EDS spectrum of PPF-3 nanosheets, XRD pattern, FESEM images of bulk 3D MOFs and the corresponding elemental mappings, nitrogen adsorption−desorption of PPF-3 nanosheets and bulk 3D MOFs, EIS characterization of the modified electrode, morphology features of the DNB, the oligonucleotides sequences used in this work, comparison of different methods for Hg^{2+} analysis, and references (PDF)

■ AUTHOR INFORMATION

Corresponding Authors

*Phone: +86-23-68252277. Fax: +86-23-68253172. E-mail: yuanruo@swu.edu.cn.

*Phone: +86 23 49891969. Fax: + 86 23 61162725. E-mail: tangying@cqwu.edu.cn.

ORCID

Ruo Yuan: 0000-0003-3664-6236

Notes

The authors declare no competing financial interest.

■ ACKNOWLEDGMENTS

This work was financially supported by the National Natural Science Foundation of China (21775124, 21675129, 21575116, 21705013), the Chongqing Science and Technology Commission of China (cstc2017jcyjAX0282, cstc2016shmsZX20001), and the Chongqing Key Laboratory of Environmental Materials and Remediation Technology (Chongqing University of Arts and Sciences) (CEK1801).

■ REFERENCES

(1) Goodman, R. P.; Heilemann, M.; Doose, S.; Erben, C. M.; Kapanidis, A. N.; Turberfield, A. J. *Nat. Nanotechnol.* **2008**, *3*, 93.

(2) Conway, J. W.; Madwar, C.; Edwardson, T. G.; McLaughlin, C. K.; Fahkoury, J.; Lennox, R. B.; Sleiman, H. F. *J. Am. Chem. Soc.* **2014**, *136*, 12987−12997.

(3) Bujold, K. E.; Hsu, J. C. C.; Sleiman, H. F. *J. Am. Chem. Soc.* **2016**, *138*, 14030−14038.

(4) Zhang, P.; Jiang, J.; Yuan, R.; Zhuo, Y.; Chai, Y. *J. Am. Chem. Soc.* **2018**, *140*, 9361−9364.

(5) Zhang, L.; Abdullah, R.; Hu, X.; Bai, H.; Fan, H.; He, L.; Liang, H.; Zou, J.; Liu, Y.; Sun, Y.; Zhang, X.; Tan, W. *J. Am. Chem. Soc.* **2019**, *141*, 4282−4290.

(6) Ling, P.; Lei, J.; Zhang, L.; Ju, H. *Anal. Chem.* **2015**, *87*, 3957−3963.

(7) Li, H.; Arroyo-Currás, N.; Kang, D.; Ricci, F.; Plaxco, K. W. *J. Am. Chem. Soc.* **2016**, *138*, 15809−15812.

(8) Ling, P.; Lei, J.; Ju, H. *Anal. Chem.* **2016**, *88*, 10680−10686.

(9) Lotfi Zadeh Zhad, H. R.; Lai, R. Y. *Anal. Chem.* **2017**, *89*, 13342−13348.

(10) Li, C.; Wu, D.; Hu, X.; Xiang, Y.; Shu, Y.; Li, G. *Anal. Chem.* **2016**, *88*, 7583−7590.

(11) Liu, S.; Fang, L.; Wang, Y.; Wang, L. *Anal. Chem.* **2017**, *89*, 3108−3115.

(12) Li, H.; Somerson, J.; Xia, F.; Plaxco, K. W. *Anal. Chem.* **2018**, *90*, 10641−10645.

(13) Peng, L. C.; Zhang, P.; Chai, Y. Q.; Yuan, R. *Anal. Chem.* **2017**, *89*, 5036−5042.

(14) Idili, A.; Amodio, A.; Vidonis, M.; Feinberg-Somerson, J.; Castronovo, M.; Ricci, F. *Anal. Chem.* **2014**, *86*, 9013−9019.

(15) Yang, M.; Zhang, X.; Liu, H.; Kang, H.; Zhu, Z.; Yang, W.; Tan, W. *Anal. Chem.* **2015**, *87*, 5854−5859.

(16) Xiong, E.; Li, Z.; Zhang, X.; Zhou, J.; Yan, X.; Liu, Y.; Chen, J. *Anal. Chem.* **2017**, *89*, 8830−8835.

(17) Monserud, J. H.; Schwartz, D. K. *ACS Nano* **2014**, *8*, 4488−4499.

(18) Das, P.; Zafar, S. *ACS Nano* **2015**, *9*, 7466−7478.

(19) Pei, H.; Lu, N.; Wen, Y.; Song, S. P.; Liu, Y.; Yan, H.; Fan, C. H. *Adv. Mater.* **2010**, *22*, 4754−4758.

(20) Lin, M.; Wen, Y.; Li, L.; Pei, H.; Liu, G.; Song, H.; Zuo, X.; Fan, C.; Huang, Q. *Anal. Chem.* **2014**, *86*, 2285−2288.

(21) Li, C.; Hu, X.; Lu, J.; Mao, X.; Xiang, Y.; Shu, Y.; Li, G. *Chem. Sci.* **2018**, *9*, 979−984.

(22) Chen, X.; Zhou, G.; Song, P.; Wang, J.; Gao, J.; Lu, J.; Fan, C.; Zuo, X. *Anal. Chem.* **2014**, *86*, 7337−7342.

(23) Song, P.; Li, M.; Shen, J.; Pei, H.; Chao, J.; Su, S.; Aldalbahi, A.; Wang, L.; Shi, J.; Song, S.; Wang, L.; Fan, C.; Zuo, X. *Anal. Chem.* **2016**, *88*, 8043−8049.

(24) Zhou, W.; Saran, R.; Liu, J. *Chem. Rev.* **2017**, *117*, 8272−8325.

(25) Yang, J.; Yang, T.; Wang, X. Y.; Chen, M.; Yu, Y.; Wang, J. *Anal. Chem.* **2018**, *90*, 6945−6951.

(26) Xia, S. A.; Leng, A.; Lin, Y.; Wu, L.; Tian, Y.; Hou, X.; Zheng, C. *Anal. Chem.* **2019**, *91*, 2701−2709.

(27) Fang, Y.; Pan, Y.; Li, P.; Xue, M.; Pei, F.; Yang, W.; Ma, N.; Hu, Q. *Food Chem.* **2016**, *213*, 609−615.

(28) Wang, S.; Lin, B.; Chen, L.; Li, N.; Xu, J.; Wang, J.; Yang, Y.; Qi, Y.; She, Y.; Shen, X.; Xiao, X. *Anal. Chem.* **2018**, *90*, 11764−11769.

(29) Miao, Y.; Sun, X.; Lv, J.; Yan, G. *Anal. Chem.* **2019**, *91*, 5036−5042.

(30) Chen, Z.; Wang, X.; Cheng, X.; Yang, W.; Wu, Y.; Fu, F. *Anal. Chem.* **2018**, *90*, 5489−5495.

(31) He, W.; Luo, L.; Liu, Q.; Chen, Z. *Anal. Chem.* **2018**, *90*, 4770−4775.

(32) Zheng, Y.; Wang, X.; He, S.; Gao, Z.; Di, Y.; Lu, K.; Li, K.; Wang, J. *Biosens. Bioelectron.* **2019**, *126*, 261−268.

(33) Akbari Hasanjani, H. R.; Zarei, K. *Biosens. Bioelectron.* **2019**, *128*, 1−8.

(34) Suherman, A. L.; Ngamchuea, K.; Tanner, E. E. L.; Sokolov, S. V.; Holter, J.; Young, N. P.; Compton, R. G. *Anal. Chem.* **2017**, *89*, 7166−7173.

(35) Li, Y.; Chang, Y.; Ma, J.; Wu, Z.; Yuan, R.; Chai, Y. *Anal. Chem.* **2019**, *91*, 6127−6133.

(36) Cao, F.; Zhao, M.; Yu, Y.; Chen, B.; Huang, Y.; Yang, J.; Cao, X.; Lu, Q.; Zhang, X.; Zhang, Z.; Tan, C.; Zhang, H. *J. Am. Chem. Soc.* **2016**, *138*, 6924−6927.

(37) Li, R.; Zhang, F.; Wang, D.; Yang, J.; Li, M.; Zhu, J.; Zhou, X.; Han, H.; Li, C. *Nat. Commun.* **2013**, *4*, 1432.

DOI: 10.1021/acs.analchem.9b03627
Anal. Chem. 2020, 92, 1811−1817

(38) Huang, Y.; Zhao, M.; Han, S.; Lai, Z.; Yang, J.; Tan, C.; Ma, Q.; Lu, Q.; Chen, J.; Zhang, X.; Zhang, Z.; Li, B.; Chen, B.; Zong, Y.; Zhang, H. *Adv. Mater.* **2017**, *29*, 1700102.
(39) Zhao, W.; Zhang, C.; Geng, F.; Zhuo, S.; Zhang, B. *ACS Nano* **2014**, *8*, 10909−10919.

DOI: 10.1021/acs.analchem.9b03627
Anal. Chem. 2020, 92, 1811−1817